Article

3D Sparse SAR Image Reconstruction Based on Cauchy Penalty and Convex Optimization

Yangyang Wang [1], Zhiming He [1], Fan Yang [2,3,*], Qiangqiang Zeng [1] and Xu Zhan [1]

1   School of Information and Communication Engineering, University of Electronic Science and Technology of China, Chengdu 611731, China; yangyangw@std.uestc.edu.cn (Y.W.); zmhe@uestc.edu.cn (Z.H.); 202022011212@std.uestc.edu.cn (Q.Z.); zhanxu@std.uestc.edu.cn (X.Z.)
2   Shenzhen Research Institute, University of Electronic Science and Technology of China, Shenzhen 518057, China
3   School of Physics and Electronic Information, Inner Mongolia Normal University, Hohhot 010028, China
*   Correspondence: nmgyangfan@imnu.edu.cn

Abstract: Three-dimensional (3D) synthetic aperture radar (SAR) images can provide comprehensive 3D spatial information for environmental monitoring, high dimensional mapping and radar cross sectional (RCS) measurement. However, the SAR image obtained by the traditional matched filtering (MF) method has a high sidelobe and is easily disturbed by noise. In order to obtain high-quality 3D SAR images, sparse signal processing has been used in SAR imaging in recent years. However, the typical L_1 regularization model is a biased estimation, which tends to underestimate the target intensity. Therefore, in this article, we present a 3D sparse SAR image reconstruction method combining the Cauchy penalty and improved alternating direction method of multipliers (ADMM). The Cauchy penalty is a non-convex penalty function, which can estimate the target intensity more accurately than L_1. At the same time, the objective function maintains convexity via the convex non-convex (CNC) strategy. Compared with L_1 regularization, the proposed method can reconstruct the image more accurately and improve the image quality. Finally, three indexes suitable for SAR images are used to evaluate the performance of the method under different conditions. Simulation and experimental results verify the effectiveness of the proposed method.

Keywords: three-dimensional (3D); synthetic aperture radar (SAR); non-convex Cauchy penalty; convex optimization

1. Introduction

Synthetic aperture radar (SAR) has the characteristics of all-time and all-weather. It can work under extreme conditions. Therefore, it is widely used in environmental monitoring [1,2], remote sensing [3–6] and radar cross sectional (RCS) measurement [7]. With the development of the SAR system, three-dimensional (3D) SAR imaging with complete spatial information has attracted the attention of researchers [8,9]. Array resolution can be achieved by the virtual two-dimensional array that can be obtained through the movement of the linear array in the horizontal and vertical directions. This ensures that the SAR system can obtain the echo data of the observation target zone. In recent years, some publicly available SAR datasets have been provided for different applications. In [10], two datasets, OpenSARShip [11] and SAR Ship Detection Dataset (SSDD) [12], were mentioned, which were used for ship detection applications [13]. In addition, a SAR database, 3DRIED, was provided for classification and 3D imaging applications [14]. The main problem is that the image quality of traditional matched filtering (MF) is poor, include sidelobe and noise interference [15]. This will have an adverse impact on subsequent image applications, such as target detection and image interpretation. Therefore, it is very significant to further improve the image quality.

Estimating the target of interest from the measured data belongs to the inverse problem of imaging. The inverse problem of SAR imaging is usually ill posed nature [16]. Therefore, the prior information of the target plays a crucial role in solving the inverse problem, which can be realized by regularization method [17,18]. The well-known regularization functions include L_1 and total variation (TV). In [19], L_1 regularization was used for SAR imaging for the first time. Then, in [17], a two-dimensional (2D) SAR imaging model based on L_1 regularization was proposed. When L_1 is applied to SAR imaging, sidelobe and noise can be effectively suppressed. As an efficient sparse reconstruction tool, L_1 regularization can be solved by many algorithms, such as iterative shrinkage and threshold algorithm (IST) [20], fast iterative shrinkage and threshold algorithm (FIST) [21] and alternating direction method of multipliers (ADMM) [22]. However, L_1 regularization is a biased estimation which tends to underestimate the amplitude of targets, especially weak scattering targets [23,24].

Therefore, the non-convex penalty function is considered to be used for diverse imaging problems. In recent years, some non-convex penalty functions have been presented for different problems, such as smooth clipped absolute deviation (SCAD) [25], minimax convex penalty (MCP) [26], the non-convex log-sum non-convex sparsity penalty [27,28] and L_q penalty term [29,30]. Compared with convex penalty functions L_1, non-convex penalty functions can usually produce more accurate estimates. However, the non-convex penalty function will lead to the non-convex objective function, which will produce sub-optimal local solutions [31]. This is the price of using non-convex penalty functions. To solve the above problems, a convex non-convex (CNC) strategy is proposed to maintain the convexity of the objective function while using the non-convex penalty function [32]. The penalty function in CNC strategy is non-convex, which can reduce the estimation deviation. At the same time, by setting the parameters of the penalty function, the objective function can maintain convexity. In [33], a sparse tight-frame regularization was used for 1D and 2D signal denoising, which maintained the convexity of the objective function via constraining the parameter of the non-convex penalty. In [34], the parameterized non-convex regularizer was used to effectively induce sparsity of the gradient magnitudes and ensured the convexity of the objective function. In [35,36], the Moreau envelope was used to define a penalty that maintains the convexity of the objective function, which was implemented using forward backward splitting. After that, CNC was further developed and applied to image denoising and image reconstruction [37–39]. In [39], a proximal splitting methodology based on symmetric Cauchy distribution was proposed to realize 1D and 2D signal denoising and proves the effectiveness of Cauchy penalty function over L_1 and TV penalty function. Therefore, in this paper, we combine CNC with the non-convex Cauchy penalty function for 3D sparse SAR image reconstruction. Due to the existence of the Cauchy proximal mapping operator, we can reconstruct the 3D SAR image by using the improved ADMM.

The ADMM have been successfully applied to solve a variety of problems, such as signal and image restoration [22,40–42]. ADMM separates the primal variables in the optimization problem into multiple sub variables by using the variable splitting, and then solves each sub optimization problem alternately. Usually, the optimization problem of sub variables is easier to solve than the original optimization problem. These sub optimization problems can be solved in parallel. Therefore, ADMM is suitable for the reconstruction of large-scale and high-dimensional images. In this paper, we combine the gradient descent method with the split augmented Lagrangian shrinkage algorithm (GSALSA) to realize 3D sparse SAR image reconstruction with Cauchy penalty function. The GSALSA is an improved ADMM, which avoids matrix inversion.

The contributions of this paper are summarized as follows:

1. We present a 3D SAR image reconstruction method based on the Cauchy non-convex penalty function and improved ADMM;
2. We apply CNC strategy to 3D sparse SAR image reconstruction. Compared with L_1 penalty function, the proposed method reduces the estimation deviation. In

addition, the objective function retains convexity, which can avoid falling into local optimization;

3. We compare the proposed method with some existing penalty functions, and give qualitative and quantitative analysis. Finally, we present several simulation and experimental results that verify the promising performance of the proposed method.

The rest of this article is organized as follows. In Section 2, we introduce the Cauchy penalty function and give the conditions of CNC. In addition, the improved ADMM method is also presented, which achieves 3D SAR image reconstruction combined with Cauchy penalty function. In Section 3, we present simulation and experimental results based on real data, and evaluate the performance of the proposed method. We give some more detailed discussion in Section 4. Finally, the conclusion is presented in Section 5.

2. Cauchy Penalty Function and Improved Alternating Direction Method of Multipliers

Firstly, we briefly explain the imaging model of the array SAR system. Secondly, we introduce the non-convexity of the Cauchy penalty and the convexity of the objective function. Finally, the improved alternating direction method of multipliers is introduced.

2.1. Array SAR Imaging Model

The measurement configuration is shown in Figure 1. X is the range direction, Y is the azimuth direction, and Z is the elevation direction. The echo data **y** is obtained by scanning the target region with a planar array. The virtual array is formed by the movement of the antenna in the azimuth direction and elevation direction. High range resolution is achieved by transmitting broadband signals. The array resolution is achieved by synthetic aperture in azimuth and elevation. Due to the SAR image obtained by traditional MF having a high sidelobe and being easily disturbed by noise, the sparse reconstruction regularization method is introduced to obtain high-quality SAR images.
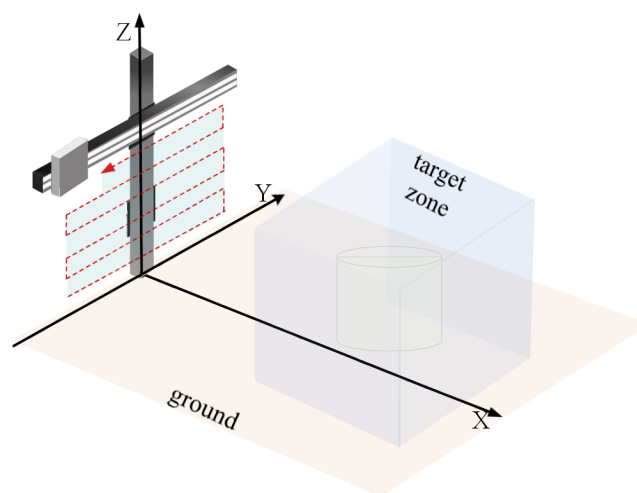
Figure 1. The measurement configuration.

The general sparse SAR image reconstruction model can be expressed as

$$\mathbf{y} = \mathbf{Dx} + \mathbf{n} \tag{1}$$

where $\mathbf{y} \in C^{M \times 1}$ is the echo data, $\mathbf{D} \in C^{M \times N}$ is the measurement matrix, $\mathbf{n} \in C^{M \times 1}$ is the noise, and $\mathbf{x} \in C^{N \times 1}$ is the reflection coefficient of the observation scene [8]. Since reconstructing **x** from **y** is an ill posed problem, we usually need to use the priori information of **x** to obtain stable reconstruction results. Under the assumption that the noise is Gaussian independent identically distributed, we can obtain the reconstruction result by solving the following optimization problem

$$\tilde{\mathbf{x}} = \min\left\{\frac{\|\mathbf{y} - \mathbf{Dx}\|_2^2}{2} + d\varphi(\mathbf{x})\right\} \qquad (2)$$

where $\varphi(\mathbf{x})$ is the penalty function, $d > 0$. In this paper, we use Cauchy penalty function, which is described in Section 2.2.

2.2. Cauchy Penalty Function

The typical penalty function used in SAR imaging is L_1 norm. The convexity of L_1 norm ensures that the optimization problem of (2) can be solved effectively. However, the L_1 norm is a biased estimation, which will underestimate the reflection coefficient of the target. The existing non-convex penalty functions, such as SCAD and MCP, can obtain more accurate solutions. However, the non-convex penalty will cause the objective function to be non-convex and fall into the sub-optimal local solution [34]. Therefore, in this paper, we introduce the convex non-convex (CNC) strategy, that is, the Cauchy penalty function is a non-convex penalty and the objective function retains convexity [39]. We present different penalty functions in Figure 2a. It can be seen that the Cauchy penalty function is non-convex. Different penalty functions correspond to different proximal mapping operators. For example, the proximal mapping operator corresponding to L_1 is a soft threshold operator. Five different proximal mapping operators are shown in Figure 2b.

(a)

(b)
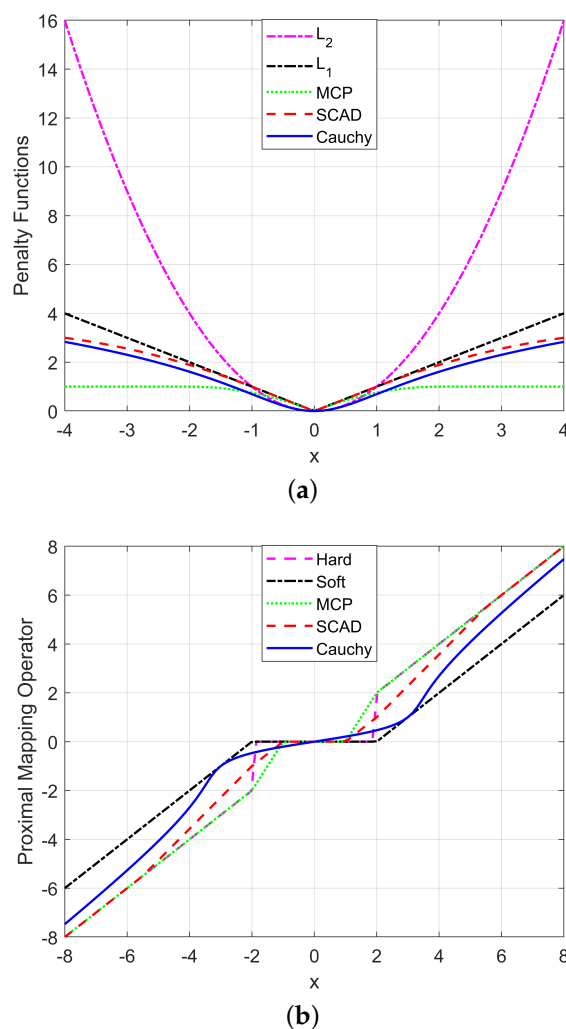
Figure 2. Different penalty functions. (**a**) Penalty functions. (**b**) Proximal mapping operators.

Cauchy distribution belongs to the case of $\alpha = 1$ in α-Stable distribution. However, unlike most α-Stable distributions, the probability density function of Cauchy distribution can be expressed analytically

$$p_c(\mathbf{x}) \propto \frac{\gamma}{\pi(\mathbf{x}^2 + \gamma^2)} \tag{3}$$

The parameter γ affects the expansion of the distribution.

Then the Cauchy penalty is

$$\varphi_c(\mathbf{x}) = -\log p_c(\mathbf{x}) = -\log\left(\frac{\gamma}{\pi(\mathbf{x}^2 + \gamma^2)}\right) \tag{4}$$

Substituting (4) into (2), the following optimization problem is obtained

$$\tilde{x} = \min\left\{ \frac{\|\mathbf{y} - \mathbf{Dx}\|_2^2}{2} - d\log\left(\frac{\gamma}{\pi(\mathbf{x}^2 + \gamma^2)}\right) \right\} \tag{5}$$

The Cauchy proximal mapping operator $\text{Pro}_{ca}(\mathbf{x}) = \min\left\{ \frac{\|\mathbf{x} - \mathbf{u}\|_2^2}{2} - \mu\varphi_c(\mathbf{x}) \right\}$ is as follows, and μ is the step size [43].

$$\begin{aligned}
\mathbf{c}_1 &= \gamma^2 + 2\mu - \frac{\mathbf{x}^2}{3} \\
\mathbf{c}_2 &= \mathbf{x}\gamma^2 + \frac{2\mathbf{x}^3}{27} - \frac{\mathbf{x}}{3}(\gamma^2 + 2\mu) \\
\mathbf{c}_3 &= \sqrt[3]{\mathbf{c}_2/2 + \sqrt{\mathbf{c}_1^3/27 + \mathbf{c}_2^2/4}} \\
\mathbf{c}_4 &= \sqrt[3]{\mathbf{c}_2/2 - \sqrt{\mathbf{c}_1^3/27 + \mathbf{c}_2^2/4}} \\
\mathbf{h} &= \frac{\mathbf{x}}{3} + \mathbf{c}_3 + \mathbf{c}_4
\end{aligned} \tag{6}$$

where $\mathbf{h}$ is the output of the Cauchy proximal mapping operator.

Next, the condition of the objective function maintains convexity is explained. We give the first-order derivative $\varphi_c'(\mathbf{x})$ and second-order derivative $\varphi_c''(\mathbf{x})$ of the function $\varphi_c(\mathbf{x})$.

$$\begin{aligned}
\varphi_c'(\mathbf{x}) &= 2\mathbf{x}/(\mathbf{x}^2 + \gamma^2) \\
\varphi_c''(\mathbf{x}) &= 2(\gamma^2 - \mathbf{x}^2)/(\mathbf{x}^2 + \gamma^2)^2
\end{aligned} \tag{7}$$

We can get $\varphi_c'(0^+) = \varphi_c'(0^-) = 0$, $\varphi_c''(0^+) = \varphi_c''(0^-) = 2/\gamma^2$. Therefore, the Cauchy penalty function is quadratic differentiable. After that, we define the objective function as follows

$$J(\mathbf{x}) = \frac{\|\mathbf{y} - \mathbf{Dx}\|_2^2}{2} - d\log\left(\frac{\gamma}{\pi(\mathbf{x}^2 + \gamma^2)}\right) \tag{8}$$

The Hessian of $J(\mathbf{x})$ is as follows

$$\nabla^2 J(\mathbf{x}) = \mathbf{D}^H\mathbf{D} + \frac{2d(\gamma^2 - \mathbf{x}^2)}{(\mathbf{x}^2 + \gamma^2)^2} \tag{9}$$

In order to keep function $J(\mathbf{x})$ convex, $\nabla^2 J(\mathbf{x}) \succeq 0$ is required

$$\mathbf{D}^H\mathbf{D} + \frac{2d(\gamma^2 - \mathbf{x}^2)}{(\mathbf{x}^2 + \gamma^2)^2} \succeq 0 \tag{10}$$

Let $\mathbf{D}^H\mathbf{D} \approx c\mathbf{I}$, $\mathbf{I}$ is the identity matrix and $c > 0$ is the constant, then there is the following relationship

$$c\mathbf{I} + \frac{2d(\gamma^2 - \mathbf{x}^2)}{\mathbf{x}^4 + 2\gamma^2\mathbf{x}^2 + \gamma^4} \succeq 0 \tag{11}$$

$$\frac{2d\left(\gamma^2 - \mathbf{x}^2\right) + c\left(\mathbf{x}^4 + 2\gamma^2\mathbf{x}^2 + \gamma^4\right)}{\left(\mathbf{x}^4 + 2\gamma^2\mathbf{x}^2 + \gamma^4\right)} \succeq 0 \tag{12}$$

$$2d\gamma^2 - 2d\mathbf{x}^2 + c\mathbf{x}^4 + 2c\gamma^2\mathbf{x}^2 + c\gamma^4 \succeq 0 \tag{13}$$

By integrating the square term on the left side of (13), the (15) is obtained

$$c\mathbf{x}^4 + 2\sqrt{c}\mathbf{x}^2\left(\sqrt{c}\gamma^2 - \frac{d}{\sqrt{c}}\right) + \left(c\gamma^4 - 2d\gamma^2 + \frac{d^2}{c}\right) + \left(4d\gamma^2 - \frac{d^2}{c}\right) \succeq 0 \tag{14}$$

$$\left(\sqrt{c}\mathbf{x}^2 + \left(\sqrt{c}\gamma^2 - \frac{d}{\sqrt{c}}\right)\right)^2 + \sigma^2\left(4\gamma^2 - \frac{d}{c}\right) \succeq 0 \tag{15}$$

Then the following inequalitie is obtained

$$4\gamma^2 - \frac{d}{c} \geq 0 \tag{16}$$

The condition for the convexity of the objective function $J(\mathbf{x})$ is

$$\gamma \geq \sqrt{d/4c} \tag{17}$$

The above conditions require $\mathbf{D}^H\mathbf{D}$ to be in diagonal form. For more general cases, the Cauchy proximal mapping operator objective function $J_2(\mathbf{u}) = \frac{\|\mathbf{x}-\mathbf{u}\|_2^2}{2} - \mu\varphi_c(\mathbf{u})$ can maintain convexity by parameter setting. The derivation process of preserving the convexity of $J_2(\mathbf{u})$ is similar to the above derivation process. Finally, it is obtained that the condition of preserving convexity is $\gamma \geq \sqrt{\mu}/2$.

2.3. Improved Alternating Direction Method of Multipliers

Firstly, we give a brief description of variable splitting. Consider the following optimization problem, which consists of two functions

$$\text{minimize} \quad f_1(\mathbf{a}) + f_2(p(\mathbf{a})) \tag{18}$$

The core idea of variable splitting is to create a new variable $\mathbf{v}$ and impose the constraints $\mathbf{v} = p(\mathbf{a})$ on the function $f_2(\cdot)$. Therefore, there is the following optimization problem

$$\begin{aligned} \text{minimize} \quad & f_1(\mathbf{a}) + f_2(\mathbf{v}) \\ \text{subject to} \quad & \mathbf{v} = p(\mathbf{a}) \end{aligned} \tag{19}$$

It is equivalent to the unconstrained optimization problem (18). The reason for variable splitting is that solving a constrained optimization problem (19) is usually simpler than solving an unconstrained optimization problem (18).

Next, we will explain the augmented Lagrange method (ALM). The augmented Lagrange multiplier method approximates the constrained optimization problem by adding a penalty term to the Lagrange function, which is zero for any feasible vector and makes it converge under more general conditions. The constrained optimization problem is as follows

$$\begin{aligned} \text{minimize} \quad & F(\mathbf{s}) \\ \text{subject to} \quad & \mathbf{Hs} - \mathbf{b} = 0 \end{aligned} \tag{20}$$

The augmented Lagrange function of (20) is

$$L_A(\mathbf{s}, \mathbf{w}, \lambda) = F(\mathbf{s}) + \mathbf{w}^H(\mathbf{b} - \mathbf{Hs}) + \frac{\lambda}{2}\|\mathbf{Hs} - \mathbf{b}\|_2^2 \tag{21}$$

where $\mathbf{w}$ is the Lagrange multiplier and $\lambda > 0$ is the penalty parameter. ALM consists of two steps: first, solve $\mathbf{s}$ by fixing $\mathbf{w}$, and then update the Lagrange multiplier $\mathbf{w}$. The above two steps are repeated until the stop condition is satisfied [44]. The general algorithm form of the ALM is shown in Algorithm 1.

Algorithm 1: ALM

Input: $k = 1$; $\mathbf{w_0}$; $\lambda > 0$.
Repeat
$\quad\quad \mathbf{s}_k \in \arg\min L_A(\mathbf{s}, \mathbf{w}_{k-1}, \lambda)$
$\quad\quad \mathbf{w}_k = \mathbf{w}_{k-1} + \lambda(\mathbf{H}\mathbf{s}_k - \mathbf{b})$
$\quad\quad k = k+1$
Until the stopping condition is satisfied

ALM also has a deformation algorithm. By sorting (21) into the form of square term and a constant, the deformation algorithm is shown in Algorithm 2.

Algorithm 2: ALM2

Input: $k = 1$; $\mathbf{w_0}$; $\lambda > 0$.
Repeat
$\quad\quad \mathbf{s}_k \in \arg\min F(\mathbf{s}) + (\lambda/2)\|\mathbf{H}\mathbf{s} - \mathbf{d}_{k-1}\|_2^2$
$\quad\quad \mathbf{d}_k = \mathbf{d}_{k-1} - (\mathbf{H}\mathbf{s}_k - \mathbf{b})$
$\quad\quad k = k+1$
Until the stopping condition is satisfied

Then, we combine ALM with variable splitting. The optimization problem becomes the following form

$$\begin{aligned} \text{minimize} \quad & f_1(\mathbf{a}) + f_2(\mathbf{v}) \\ \text{subject to} \quad & \mathbf{G}\mathbf{a} = \mathbf{v} \end{aligned} \tag{22}$$

Through the following definition, (22) can be rewritten into the form of (20)

$$\begin{aligned} F(\mathbf{s}) &= f_1(\mathbf{a}) + f_2(\mathbf{v}) \\ \mathbf{b} &= \mathbf{0}, \mathbf{H} = \begin{bmatrix} \mathbf{G} & -\mathbf{I} \end{bmatrix}, \mathbf{s} = \begin{bmatrix} \mathbf{a} \\ \mathbf{v} \end{bmatrix} \end{aligned} \tag{23}$$

The two repeated steps in Algorithm 2 become

$$\begin{aligned} (\mathbf{a}_k, \mathbf{v}_k) &\in \arg\min f_1(\mathbf{a}) + f_2(\mathbf{v}) + \tfrac{\lambda}{2}\|\mathbf{G}\mathbf{a} - \mathbf{v} - \mathbf{d}_{k-1}\|_2^2 \\ \mathbf{d}_k &= \mathbf{d}_{k-1} - (\mathbf{G}\mathbf{a}_k - \mathbf{v}_k) \end{aligned} \tag{24}$$

It is difficult to solve (24) directly. Therefore, we use ADMM to solve $\mathbf{a}$ and $\mathbf{v}$ alternately. ADMM is a special form of ALM, which uses a divide and conquer approach to transform the optimization problem of the primal variable into the multiple sub-optimization problems. These subproblems can be solved independently and in parallel, which are suitable for solving large-scale optimization problems. The main steps of ADMM are shown in Algorithm 3.

Algorithm 3: ADMM
Input: $k = 1$; $\mathbf{v}_0$; $\mathbf{d}_0$; $\lambda > 0$.
Repeat
$\quad\quad\quad \mathbf{a}_k \in \arg\min f_1(\mathbf{a}) + \frac{\lambda}{2}\|\mathbf{G}\mathbf{a} - \mathbf{v}_{k-1} - \mathbf{d}_{k-1}\|_2^2$
$\quad\quad\quad \mathbf{v}_k \in \arg\min f_2(\mathbf{v}) + \frac{\lambda}{2}\|\mathbf{G}\mathbf{a}_{k-1} - \mathbf{v} - \mathbf{d}_{k-1}\|_2^2$
$\quad\quad\quad \mathbf{d}_k = \mathbf{d}_{k-1} - (\mathbf{G}\mathbf{a}_k - \mathbf{v}_k)$
$\quad\quad\quad k = k + 1$
Until the stopping condition is satisfied

The optimization problem of SAR image reconstruction (2) can be written as follows

$$f_1(\mathbf{x}) = \frac{1}{2}\|\mathbf{y} - \mathbf{D}\mathbf{x}\|_2^2, f_2(\mathbf{x}) = \varphi_c(\mathbf{x}), \mathbf{G} = \mathbf{I} \tag{25}$$

$$\begin{array}{ll} \text{minimize} & \frac{1}{2}\|\mathbf{y} - \mathbf{D}\mathbf{x}\| + d\varphi_c(\mathbf{v}) \\ \text{subject to} & \mathbf{x} = \mathbf{v} \end{array} \tag{26}$$

A variant of the ADMM algorithm, SALSA, is proposed to solve the above optimization problem [40]. The main steps of SALSA are shown in Algorithm 4.

Algorithm 4: SALSA
Input: $k = 1$; $\mathbf{v}_0$; $\mathbf{d}_0$; $\lambda > 0$.
Repeat
$\quad\quad\quad \mathbf{x}_k \in \arg\min\|\mathbf{y} - \mathbf{D}\mathbf{x}\|_2^2 + \lambda\|\mathbf{x} - \mathbf{v}_{k-1} - \mathbf{d}_{k-1}\|_2^2$
$\quad\quad\quad \Rightarrow \left(\mathbf{D}^H\mathbf{D} + \lambda\mathbf{I}\right)^{-1}\left(\mathbf{D}^H\mathbf{y} + \lambda(\mathbf{v}_{k-1} + \mathbf{d}_{k-1})\right)$
$\quad\quad\quad \mathbf{v}_k \in \arg\min \varphi_c(\mathbf{x}) + \frac{\lambda}{2}\|\mathbf{x}_{k-1} - \mathbf{v} - \mathbf{d}_{k-1}\|_2^2$
$\quad\quad\quad \mathbf{d}_k = \mathbf{d}_{k-1} - (\mathbf{a}_k - \mathbf{v}_k)$
$\quad\quad\quad k = k + 1$
Until the stopping condition is satisfied

In Algorithm 4, the first sub-optimization problem involves matrix inversion, which brings high computation burden. For 3D imaging, the burden is intolerable. Hence, the GSALSA is presented with two modifications to reduce the computation complexity. The first modification is to linearize the original problem [45], which can hence avoid the matrix inverse operation.

$$\begin{aligned} \mathbf{x}_k &= \text{argmin}_{\mathbf{x}_k}\|\mathbf{y} - \mathbf{D}\mathbf{x}_k\|_2^2 + \lambda\|\mathbf{x}_k - \mathbf{v}_{k-1} - \mathbf{d}_{k-1}\|_2^2 \\ &\approx \text{argmin}_{\mathbf{x}_k} f(\mathbf{x}_{k-1}) + \nabla^H f(\mathbf{x}_{k-1})(\mathbf{x}_k - \mathbf{x}_{k-1}) + L\|\mathbf{x}_k - \mathbf{x}_{k-1}\|_2^2 \\ &= \text{argmin}_{\mathbf{x}_k}\left\|\mathbf{x}_k - \mathbf{x}_{k-1} + \frac{1}{2L}\nabla^H f(\mathbf{x}_{k-1})\right\|_2^2 \end{aligned} \tag{27}$$

$$\mathbf{x}_k = \mathbf{x}_{k-1} - \frac{1}{L}\left[\lambda\mathbf{x}_{k-1} + \mathbf{D}^H(\mathbf{D}\mathbf{x}_{k-1} - \mathbf{y}) - \lambda(\mathbf{v}_{k-1} + \mathbf{d}_{k-1})\right] \tag{28}$$

The second modification is to introduce the imaging operator $I(\cdot)$ and inverse imaging operator $I^{-1}(\cdot)$. The following relationship is established, $I(\mathbf{y}) \approx \mathbf{D}^H\mathbf{y}, g(\mathbf{x}) \approx \mathbf{D}\mathbf{x}, I \cdot g \approx \mathbf{I}$. More details can be found in [46]. The research work in [7,47] shows that using the above criteria and taking the MF image data $\mathbf{y}_{MF}$ as the input, the result obtained is similar to those with echo data as input, and the calculation time is reduced. Finally, the 3D sparse SAR image reconstruction method combining Cauchy proximal mapping operator and GSALSA is shown in Algorithm 5.

Algorithm 5: GSALSA-Cauchy

Input: $k_0 = 1$; Maximum number of iterations k_{max}; Error parameter ε; $\mathbf{v}_0 = \mathbf{0}$;
$\mathbf{d}_0 = \mathbf{0}$; $\lambda > 0$.

Repeat

$$\mathbf{x}_k = \mathbf{x}_{k-1} - \frac{1}{L}[\lambda\mathbf{x}_{k-1} + I(g(\mathbf{x}_{k-1})) - \mathbf{y}_{MF} - \lambda(\mathbf{v}_{k-1} + \mathbf{d}_{k-1})]$$
$$\mathbf{v}_k = \text{Pro}_{ca}(\mathbf{x}_k - \mathbf{d}_{k-1})$$
$$\mathbf{d}_k = \mathbf{d}_{k-1} - (\mathbf{x}_k - \mathbf{v}_k)$$
$$\text{Res} = \|\mathbf{x}_k - \mathbf{x}_{k-1}\|_F$$
$$k = k + 1$$

Until Res $< \varepsilon$ or $k > k_{max}$

**Output**: $\mathbf{x}_k$

---

3. Experiments and Analysis

In this part, simulation and experiments based on real data are presented to verify the effectiveness of the proposed method. Firstly, we give the simulation results of the aircraft model which can be seen in the next subsection. Secondly, the data processing results of two different SAR systems are given. We compare the proposed method with MF, FIST, SCAD and MCP. The results of quantitative evaluation and visualization are presented, which fully verifies the effectiveness of the proposed method. We use three indicators to evaluate the performance of different methods, namely peak signal-to-noise ratio (PSNR), normalized mean square error (NMSE) [48] and the relative error (RE) [49].
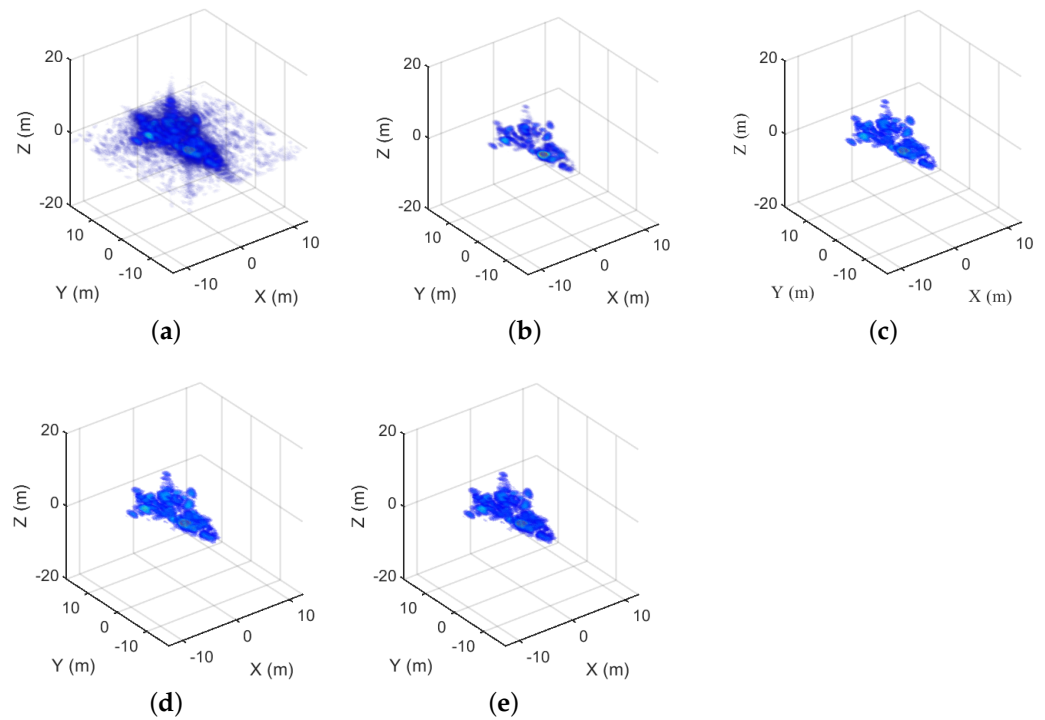
3.1. Aircraft Model

Firstly, an aircraft model is used for simulation, whose length, width and height are 16, 12 and 8 m, respectively. The main simulation parameters are as follows. the carrier frequency is 37.5 GHz and the bandwidth is 0.164 GHz. The size of the virtual scanning array is 3 m × 3 m. We fixed the SNR to 20 dB to analyze the performance of different methods. Figure 3 shows the 3D reconstruction results of MF, FIST, SCAD, MCP and GSALSA–Cauchy under full sampling conditions. Figure 4 shows the 3D reconstruction results of MF, FIST, SCAD, MCP and GSALSA–Cauchy at 75% sampling rate. The results show that the proposed method can effectively improve the quality of 3D SAR image. In addition, as expected, as the sampling rate decreases, the image quality decreases.

The index evaluation under full sampling and 75% sampling are listed in Tables 1 and 2, respectively. Under the condition of full sampling, the PSNR of FIST, SCAD, MCP and GSALSA-Cauchy are 42.9033 dB, 45.5338 dB, 45.6318 dB and 46.1380 dB, respectively. Compared with FIST, the PSNR of the proposed method is improved by about 3 dB. The NMSE of FIST, SCAD, MCP and GSALSA–Cauchy are 0.3340, 0.2026, 0.1852 and 0.1367, respectively. The NMSE of the proposed method is reduced by nearly half compared with FIST. The RE of FIST, SCAD, MCP and GSALSA–Cauchy are 2.0070, 0.2853, 0.2661 and 0.2383, respectively. It can be seen that the RE of the non-convex penalty function is significantly less than that of the L_1 penalty function.

For 75% sampling conditions, among the four different methods, the PSNR of FIST is the smallest, which is 42.3921 dB, and that of the proposed method is the highest, which is 45.0526 dB. The NMSE of the proposed method is the smallest of the four methods, which is 0.1673. The RE value of FIST is the largest, 2.0820, while that of the proposed method is only 0.2667.
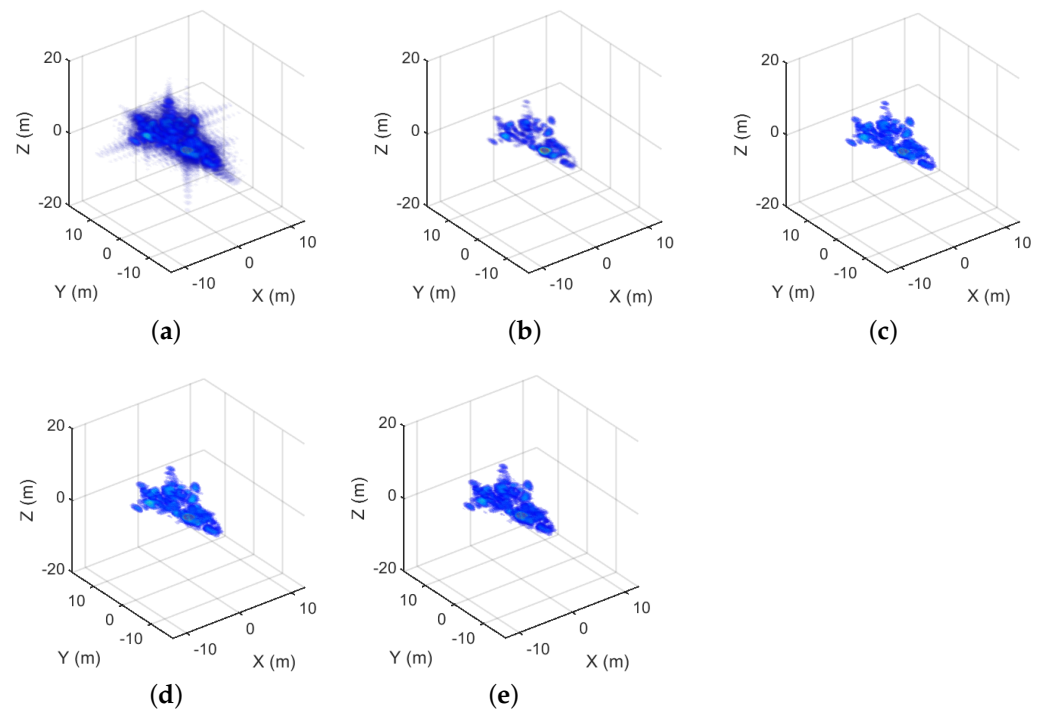
Figure 3. The imaging results of the aircraft with full sampling. (**a**) The MF result. (**b**) The FIST result. (**c**) The SCAD result. (**d**) The MCP result. (**e**) The GSALSA–Cauchy result.

Figure 4. The imaging results of the aircraft corresponding to the 75% sampling rate. (**a**) The MF result. (**b**) The FIST result. (**c**) The SCAD result. (**d**) The MCP result. (**e**) The GSALSA–Cauchy result.

**Table 1.** PSNR, NMSE and RE of aircraft model with full sampling.

Method	FIST	SCAD	MCP	GSALSA–Cauchy
PSNR	42.9033	45.5338	45.6318	46.1380
NMSE	0.3340	0.2026	0.1852	0.1367
RE	2.0070	0.2853	0.2661	0.2383

Table 2. PSNR, NMSE and RE of aircraft model under 75% sampling.

| Method	FIST	SCAD	MCP	GSALSA–Cauchy
PSNR	42.3921	44.7422	44.7776	45.0526
NMSE	0.3579	0.2316	0.2148	0.1673
RE	2.0820	0.3648	0.3466	0.2667

3.2. The Corner Reflector Experiment

The 3D measured data of the corner reflector is processed and analyzed to verify the effectiveness of the method in a real scene. The experimental scenario is shown in Figure 5a. The main parameters of the system are as follows. The center frequency is 81 GHz, and the signal bandwidth is 4 GHz. The 3D imaging results of MF, FIST, SCAD, MCP and GSALSA-Cauchy at full sampling and 75% sampling rate are shown in Figures 6 and 7, respectively. The results show that the reconstructed 3D SAR image quality is better than MF. Tables 3 and 4 list the quantitative analysis under different sampling rates.

(**a**)   (**b**)
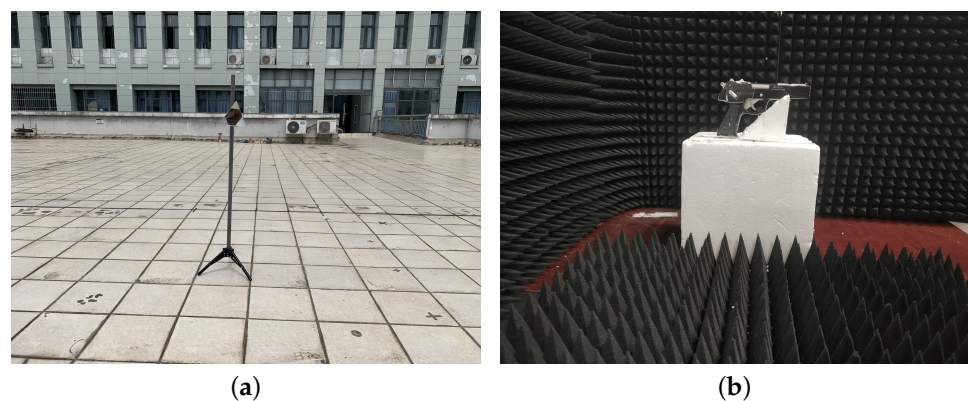
Figure 5. The experimental scenario. (**a**) The corner reflector. (**b**) The pistol.

**Table 3.** PSNR, NMSE and RE of the corner reflector with full sampling.

Method	FIST	SCAD	MCP	GSALSA–Cauchy
PSNR	39.5480	41.6442	42.1289	43.3540
NMSE	0.4860	0.3599	0.3382	0.3065
RE	2.5810	0.3913	0.3687	0.2872

Table 4. PSNR, NMSE and RE of the corner reflector with 75% sampling.

Method	FIST	SCAD	MCP	GSALSA–Cauchy
PSNR	39.4820	41.2316	42.0484	43.1757
NMSE	0.4902	0.3801	0.3729	0.3235
RE	2.6013	0.4095	0.3857	0.3165
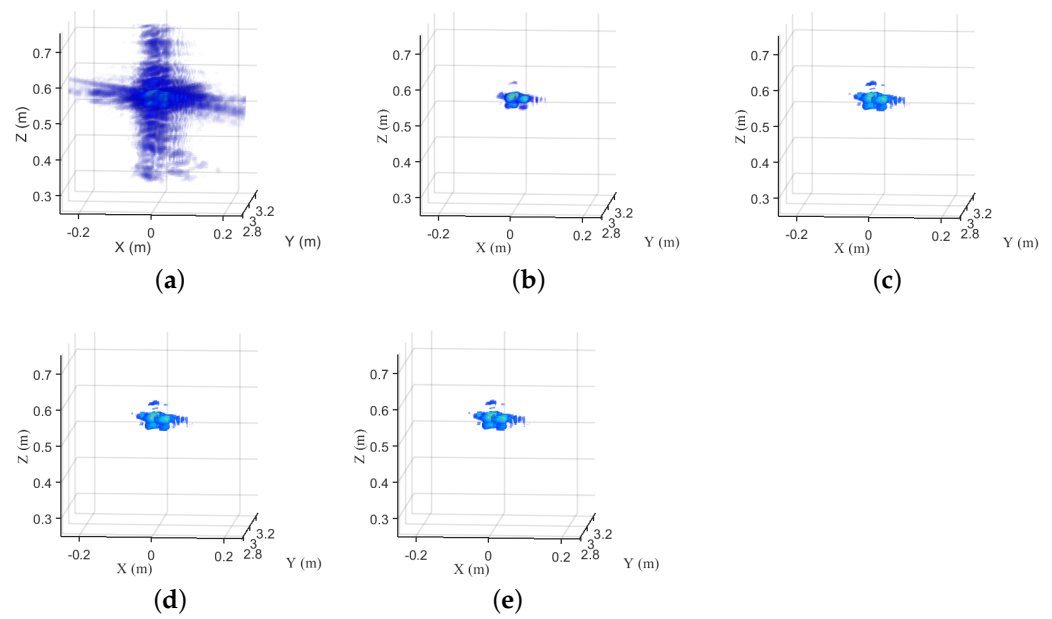
Figure 6. The imaging results of the corner reflector with full sampling. (**a**) The MF result. (**b**) The FIST result. (**c**) The SCAD result. (**d**) The MCP result. (**e**) The GSALSA–Cauchy result.
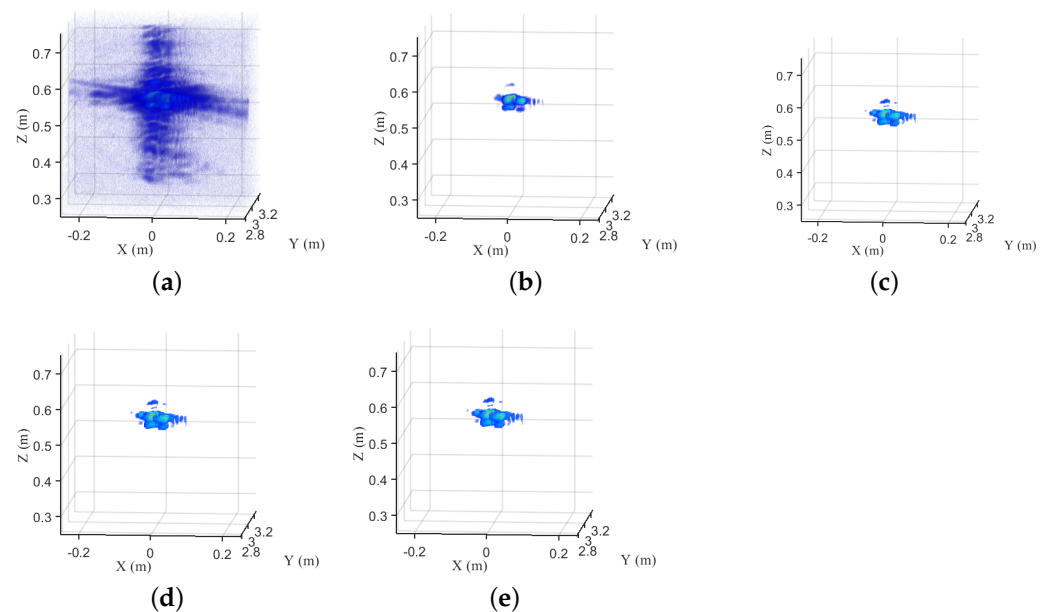
Figure 7. The imaging results of the corner reflector corresponding to the 75% sampling rate. (**a**) The MF result. (**b**) The FIST result. (**c**) The SCAD result. (**d**) The MCP result. (**e**) The GSALSA–Cauchy result.

In the case of full sampling, the PSNR of FIST, SCAD, MCP and GSALSA–Cauchy are 39.5480 dB, 41.6442 dB, 42.1289 dB and 43.3540 dB, respectively. It can be seen that the PSNR of the proposed method is the highest. For NMSE, GSALSA–Cauchy is the smallest of the four methods. The RE of FIST, SCAD, MCP and GSALSA–Cauchy are 2.5810, 0.3913, 0.3687 and 0.2872, respectively. It can be seen that the RE of GSALSA–Cauchy is the smallest, which shows the reconstruction accuracy of the proposed method is the highest compared with FIST, SCAD and MCP. For 75% sampling conditions, the PSNR of FIST, SCAD, MCP and GSALSA–Cauchy are 39.4820 dB, 41.2316 dB, 42.0484 dB and 43.1757 dB, respectively. It can be seen that the PSNR of FIST is the smallest and the PSNR of the proposed method is the highest. The NMSE of the proposed method is only 0.3235. The RE of FIST, SCAD,

MCP and GSALSA–Cauchy are 2.6013, 0.4095, 0.3857 and 0.3165, respectively. Compared with FIST, the RE of the proposed method is significantly reduced. The results show that the reconstructed image quality and accuracy of the proposed method are improved at different sampling rates.

3.3. The Experiment of Pistol

The pistol data of another SAR system are used to further analyze and verify the performance of the method. The experimental scenario is shown in Figure 5b. The main parameters of the system are as follows. The center frequency is 78.8 GHz, signal bandwidth is 3.599 GHz, and the array size is 0.4×0.4 m. Figures 8 and 9 show the 3D results of pistols at different sampling rates. It can be seen that the image quality of the MF is poor, and the sidelobe and noise are obvious in the imaging results. After sparse reconstruction of SAR image via the proposed method, the image quality is improved. The quantitative analysis at different sampling rates with PSNR, NMSE and RE is listed in Tables 5 and 6. At full sampling, the PSNR of FIST, SCAD, MCP and GSALSA–Cauchy are 37.6217 dB, 40.2308 dB, 40.9578 dB and 41.4718 dB, respectively. Compared with FIST, the PSNR of the proposed method is improved by approximately 3 dB. The NMSE of FIST, SCAD, MCP and GSALSA–Cauchy are 0.1442, 0.1038, 0.0712 and 0.0524, respectively. Among the four methods, the RE of the proposed method is the smallest, only 0.1703, which shows that the reconstruction accuracy of the GSALSA–Cauchy is higher than that of the other three methods.

When the sampling rate is 75%, the performance of GSALSA–Cauchy is also better than that of FIST. The PSNR, NMSE and RE of FIST are 34.8553dB, 0.2473 and 2.3088, respectively, while the PSNR, NMSE and RE of GSALSA-Cauchy are 37.2201dB, 0.1592 and 0.3359, respectively. Simulation and real data experiments show that the proposed method can reconstruct 3D SAR images more accurately.
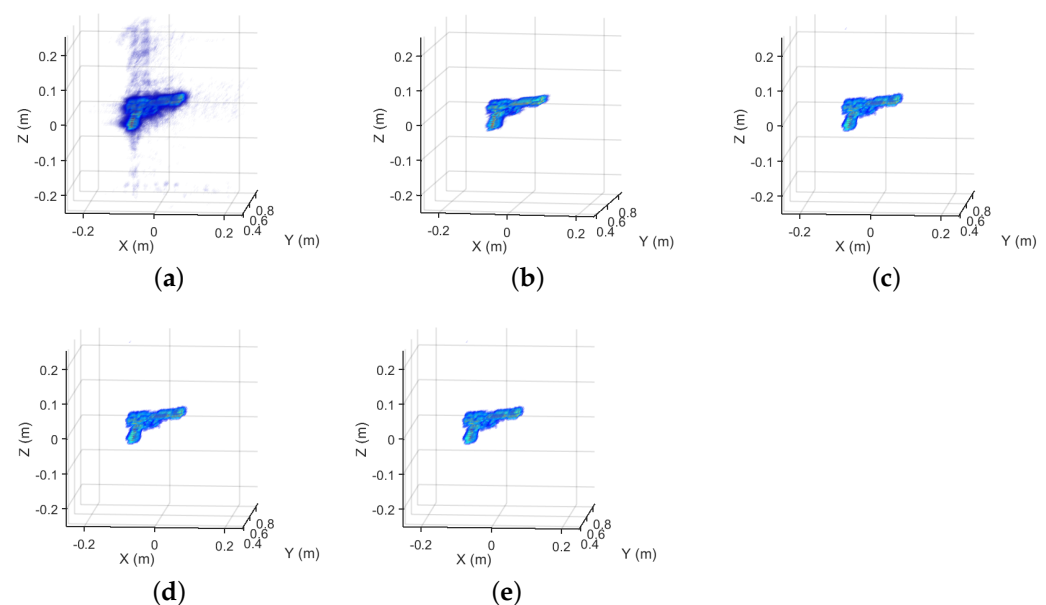
Figure 8. The imaging results of the pistol with full sampling. (**a**) The MF result. (**b**) The FIST result. (**c**) The SCAD result. (**d**) The MCP result. (**e**) The GSALSA–Cauchy result.
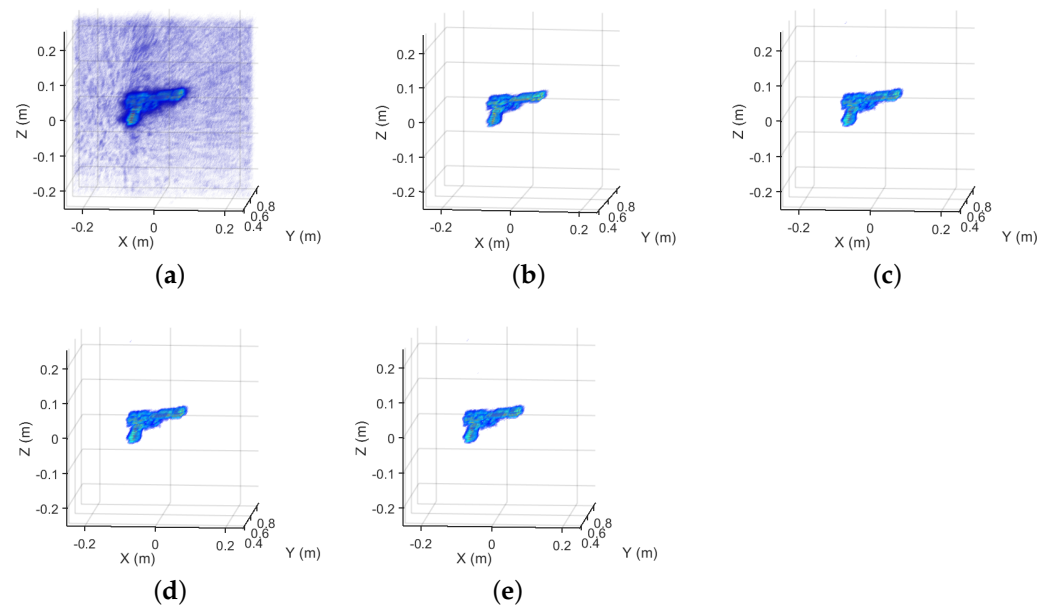
Figure 9. The imaging results of the pistol corresponding to the 75% sampling rate. (**a**) The MF result. (**b**) The FIST result. (**c**) The SCAD result. (**d**) The MCP result. (**e**) The GSALSA–Cauchy result.

Table 5. PSNR, NMSE and RE of pistol model with full sampling.

Method	FIST	SCAD	MCP	GSALSA–Cauchy
PSNR	37.6217	40.2308	40.9578	41.4718
NMSE	0.1442	0.1038	0.0712	0.0524
RE	1.6972	0.2386	0.1925	0.1703

Table 6. PSNR, NMSE and RE of pistol model under 75% sampling.

| Method	FIST	SCAD	MCP	GSALSA–Cauchy
PSNR	34.8553	36.1121	36.4466	37.2201
NMSE	0.2473	0.2104	0.1793	0.1592
RE	2.3088	0.3854	0.3693	0.3359

4. Discussion

In this part, we analyze the imaging results and the method performance under different SNR conditions. Figures 10 and 11 show the aircraft imaging results with SNR of 15 dB and 10 dB, respectively. The results show that the image quality and reconstruction accuracy of the proposed method are improved compared with L_1 regularization. The performance deterioration caused by the reduction in SNR cannot be visually reflected. Therefore, we list the quantitative analysis in Table 7. It can be seen that with the decrease in SNR, the PSNR of the four methods decreases, and the NMSE and RE increase. Nevertheless, under different SNR conditions, the performance of GSALSA–Cauchy is still better than FIST, SCAD and MCP.

Additionally, we analyze the performance of the method at lower sampling rates (50% and 25%). The imaging results are shown in Figures 12 and 13. As the sampling rate decreases, the image quality also decreases, which is consistent with the quantitative analysis in Tables 8 and 9. Although the image quality decreases with the decrease in sampling rate, the image quality of the proposed method is significantly improved compared with MF. Compared with L_1 regularization, GSALSA–Cauchy can reconstruct the image more accurately.
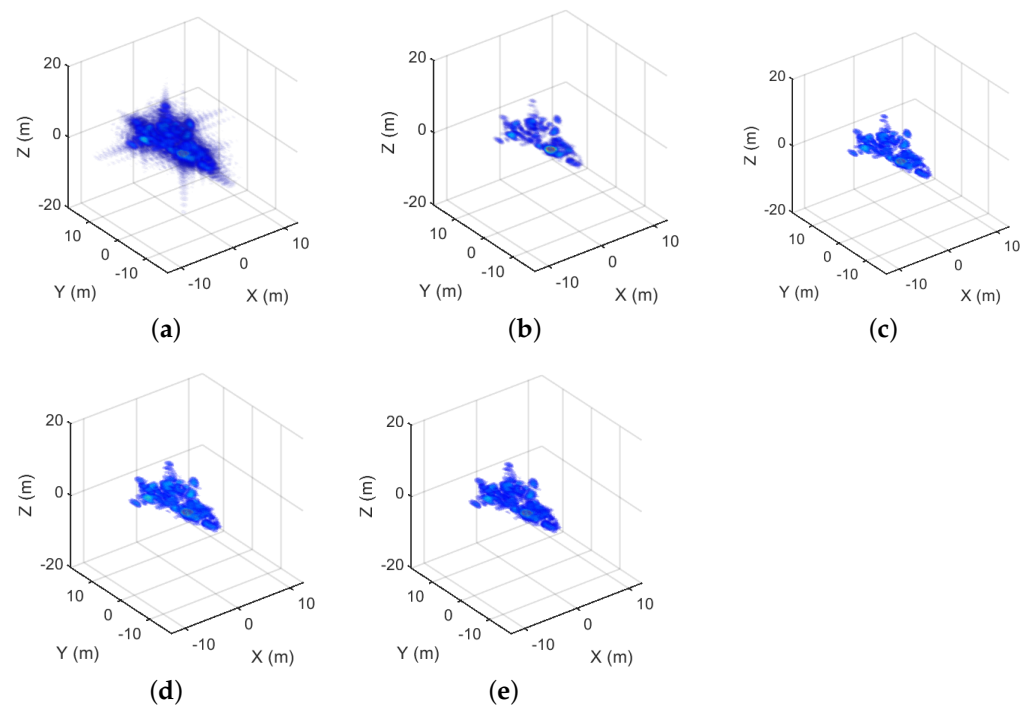
Figure 10. The imaging results of the aircraft with SNR of 15 dB. (**a**) The MF result. (**b**) The FIST result. (**c**) The SCAD result. (**d**) The MCP result. (**e**) The GSALSA–Cauchy result.
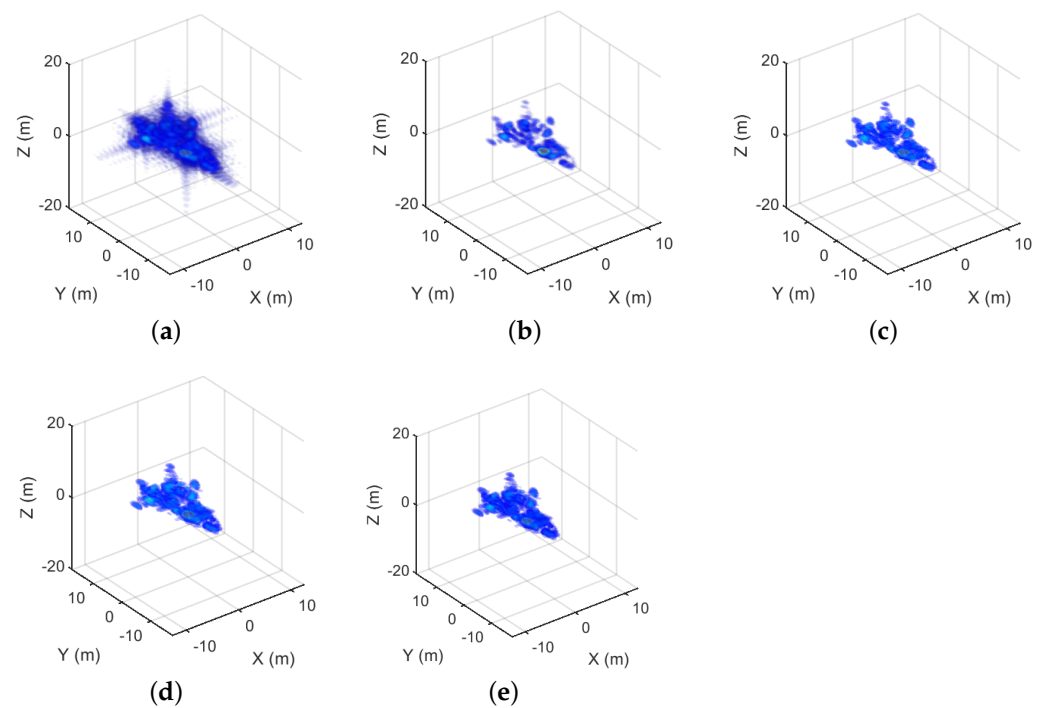
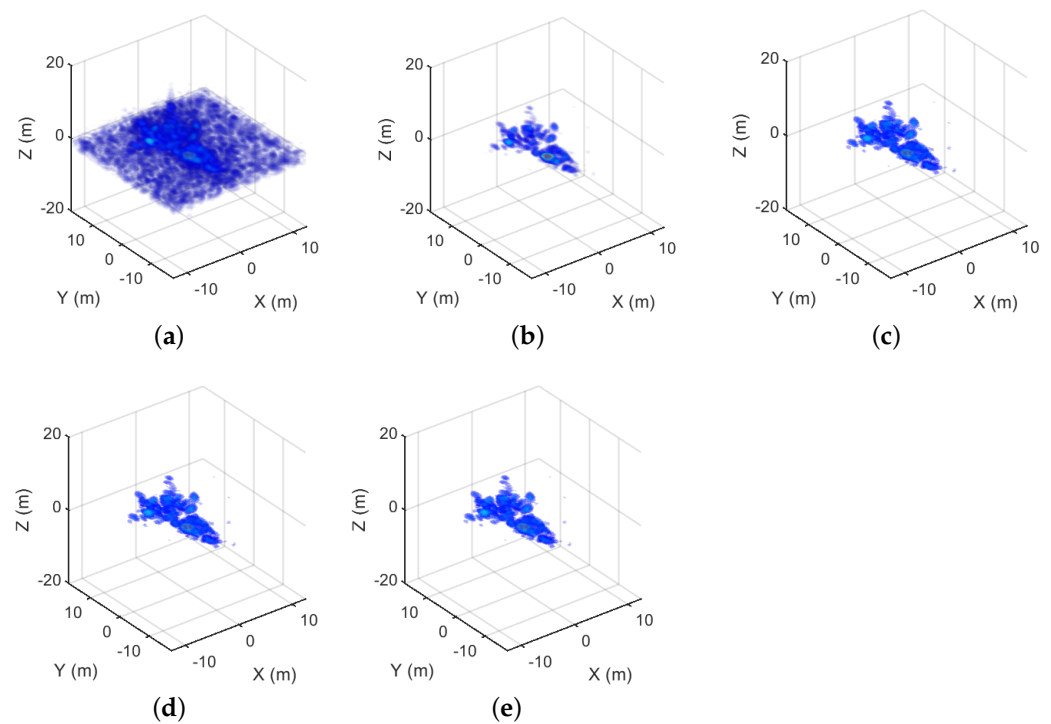**Figure 11.** The imaging results of the aircraft with SNR of 10 dB. (**a**) The MF result. (**b**) The FIST result. (**c**) The SCAD result. (**d**) The MCP result. (**e**) The GSALSA–Cauchy result.
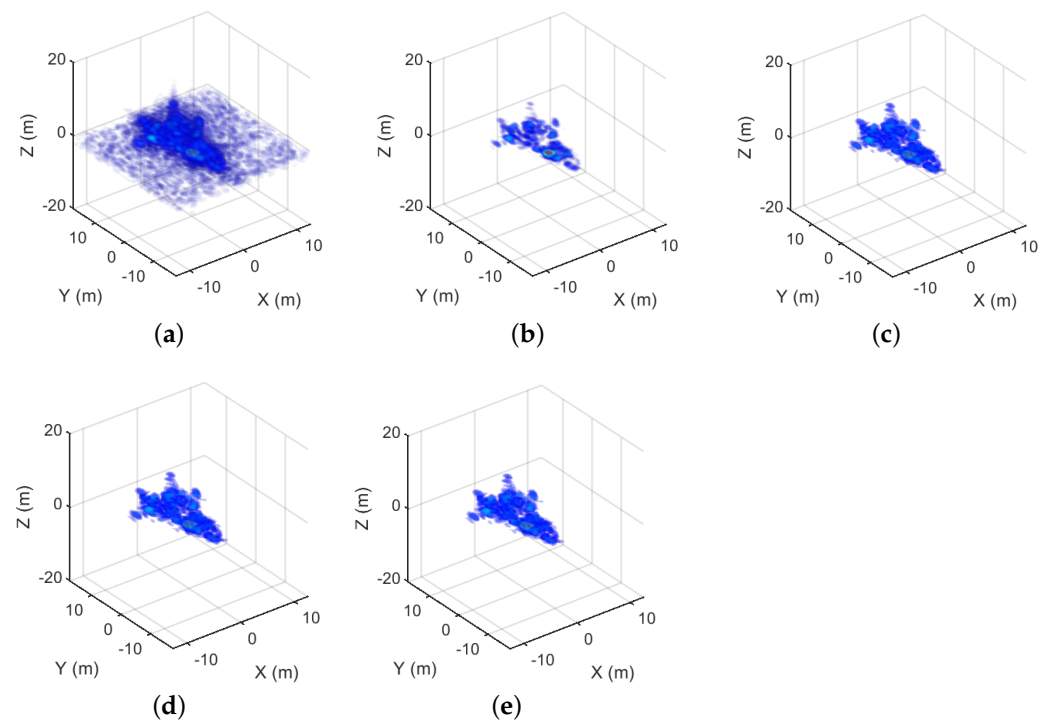
Figure 12. The imaging results of aircraft corresponding to the 50% sampling. (**a**) The MF result. (**b**) The FIST result. (**c**) The SCAD result. (**d**) The MCP result. (**e**) The GSALSA–Cauchy result.

Figure 13. The imaging results of aircraft corresponding to the 25% sampling. (**a**) The MF result. (**b**) The FIST result. (**c**) The SCAD result. (**d**) The MCP result. (**e**) The GSALSA–Cauchy result.

Table 7. PSNR, NMSE and RE of aircraft model under different SNR.

SNR	Method	PSNR	NMSE	RE
20	FIST	42.9033	0.3340	2.0070
	SCAD	45.5338	0.2026	0.2853
	MCP	45.6318	0.1852	0.2661
	GSALSA–Cauchy	46.1380	0.1367	0.2383
15	FIST	42.8691	0.3360	2.0079
	SCAD	45.4755	0.2049	0.2989
	MCP	45.5686	0.1876	0.2724
	GSALSA–Cauchy	46.0555	0.1391	0.2465
10	FIST	42.7557	0.3417	2.0264
	SCAD	44.9194	0.2118	0.3399
	MCP	45.2047	0.1944	0.2907
	GSALSA–Cauchy	45.7885	0.1465	0.2786
5	FIST	42.4084	0.3578	2.0773
	SCAD	44.7494	0.2320	0.4236
	MCP	44.7860	0.2151	0.3473
	GSALSA–Cauchy	45.0355	0.1685	0.3227
0	FIST	41.4968	0.4082	2.2554
	SCAD	43.0364	0.2922	0.5921
	MCP	43.3931	0.2771	0.5004
	GSALSA–Cauchy	43.6851	0.2332	0.4721

Table 8. PSNR, NMSE and RE of aircraft model under 50% sampling.

Method	FIST	SCAD	MCP	GSALSA–Cauchy
PSNR	41.6101	43.2581	43.5891	43.6651
NMSE	0.3994	0.2788	0.2632	0.2146
RE	2.2343	0.5095	0.4844	0.4623

Table 9. PSNR, NMSE and RE of aircraft model under 25% sampling.

Method	FIST	SCAD	MCP	GSALSA–Cauchy
PSNR	40.0131	41.2218	41.3731	41.4339
NMSE	0.4939	0.3728	0.3660	0.2953
RE	2.5984	0.5992	0.5865	0.4767

Then, we illustrate the computational complexity of the algorithm. All the above algorithms' computation complexities are summarized in Table 10. The related details can be found in the Appendix A. From the summarization, it can be seen that the proposed algorithm has the lowest complexity. Compared with Algorithm 4, the improved one reduces the complexity from $O\left(\left(N_x N_y N_z\right)^3\right)$ to $O\left(N_x N_y N_z\right)$.

Table 10. Computational complexity of different algorithms.

ALM	ALM2	ADMM	SALSA	GSALSA
$O\left(K\left(N_x N_y N_z\right)^2\right)$		$O\left(\left(N_x N_y N_z\right)^3\right)$		$O\left(N_x N_y N_z\right)$

Finally, there is one factor that we have not considered in the simulation, that is, there may be multiple features in the scene. Hence, we consider using multiple penalty functions to further improve the image quality in future work, which has been proved to be feasible in two-dimensional images [50].

5. Conclusions

In this article, a 3D SAR image reconstruction method combining the Cauchy penalty function and improved ADMM is proposed. Compared with the L_1 penalty function, the Cauchy penalty function is a non-convex function, which can reconstruct the image more accurately. At the same time, the objective function retains convexity, so it can avoid falling into suboptimal local solutions. In addition, we combine gradient descent with SALSA, which is suitable for solving large-scale and high-dimensional optimization problems. Finally, we make a quantitative and qualitative analysis of the proposed method. Compared with MF, the presented method can effectively improve the image quality. Compared with L_1, the estimation deviation can be reduced. The simulation and real SAR data experimental results show that this method can effectively improve the quality and reconstruction accuracy of the 3D SAR image, and is conducive to the subsequent application of the image, such as RCS measurement. Our future research work is mainly to integrate deep learning into 3D sparse SAR image reconstruction, so as to get a more automatic and efficient image reconstruction method.

Appendix A. Computation Complexities of Different Algorithm

Computation complexities of Algorithms 1–5 are analyzed as follows.

Appendix A.1. Algorithms 1 and 2

In each iteration, two sub-problems are solved. The first sub-problem is

$$\mathbf{s}_k = \mathrm{argmin}_{\mathbf{s}_k} F(\mathbf{s}) + \mathbf{w}_{k-1}^H (\mathbf{b} - \mathbf{Hs}) + \frac{\lambda}{2} \|\mathbf{b} - \mathbf{Hs}\|_2^2 \tag{A1}$$

It can be solved by proximal algorithms like forward-backward (FB) algorithm [51], which contains iterations of two steps.

$$\mathbf{s}_{k\mathrm{c}} = \mathbf{s}_{k-1} + \mu \mathbf{H}^H (\mathbf{b} - \mathbf{Hs}_{k-1}) \tag{A2}$$

$$\mathbf{s}_k^3 - \mathbf{s}_{kc} \mathbf{s}_k^2 + \left(\gamma^2 + 2\mu \right) \mathbf{s}_k - \mathbf{s}_{kc} \gamma^2 = \mathbf{0} \tag{A3}$$

The main computation burden in the first step is matrix-vector multiplication. Thus, the computation complexity is about $O\left(\left(N_x N_y N_z \right)^2 \right)$, where N_x, N_y and N_z are pixels of 3-D image along each axis. The second step is to solve a cubic function [43] that is executed pointwise as in (6). The computation complexity is about $O(N_x N_y N_z)$. Normally, for 3-D SAR imaging, according to our experience and others [8]. Thus, for this sub-problem, its total complexity is about $O\left(K \left(N_x N_y N_z \right)^2 \right)$, where K denotes the iteration times.

The second sub-problem is solved as

$$\mathbf{w}_k = \mathbf{w}_{k-1} + \lambda (\mathbf{Hs}_k - \mathbf{b}) \tag{A4}$$

The main computation burden is matrix-vector multiplication. Thus, the computation complexity is about $O\left(\left(N_xN_yN_z\right)^2\right)$.

In total, for Algorithm 1, its main computation complexity is about $O\left(K\left(N_xN_yN_z\right)^2\right)$.

Algorithm 2 is formed by emerging the linear term in (21) into the quadratic term. It's an alternative form of Algorithm 1. Thus, its computation complexity is roughly the same as Algorithm 1, which is about $O\left(K\left(N_xN_yN_z\right)^2\right)$.

Appendix A.2. Algorithms 3 and 4

Algorithm 3 is a general framework of ADMM and Algorithm 4 is the specific instance for our SAR image reconstruction. Thus Algorithm 3 and 4 share the same computation complexity. Taking Algorithm 4 for example, in each iteration, three sub-problems are solved. The first sub-problem is solved as

$$\mathbf{x}_k = \left(\mathbf{D}^\mathbf{H}\mathbf{D} + \lambda\mathbf{I}\right)^{-1}\left(\mathbf{D}^\mathbf{H}\mathbf{y} + \lambda(\mathbf{v}_{k-1} + \mathbf{d}_{k-1})\right) \tag{A5}$$

The main computation burden is matrix inverse operation, which has the complexity around $O\left(\left(N_xN_yN_z\right)^3\right)$.

The second sub-problem is

$$\mathbf{v}_k = \operatorname{argmin}_{\mathbf{v}_k}\varphi_c(\mathbf{v}) + \frac{\lambda}{2}\|\mathbf{x}_{k-1} - \mathbf{v} - \mathbf{d}_{k-1}\|_2^2 \tag{A6}$$

which can be solved via proximal operator with close-form expression as

$$\mathbf{v}_k^3 - (\mathbf{x}_{k-1} - \mathbf{d}_{k-1})\mathbf{v}_k^2 + \left(\gamma^2 + 2\mu\right)\mathbf{v}_k - (\mathbf{x}_{k-1} - \mathbf{d}_{k-1})\gamma^2 = \mathbf{0} \tag{A7}$$

Similarly, to solve this cubic function point-wise, as in (6), the solution is obtained. The computation complexity is about $O(N_xN_yN_z)$.

The third sub-problem is solved as

$$\mathbf{d}_k = \mathbf{d}_{k-1} - (\mathbf{a}_k - \mathbf{v}_k) \tag{A8}$$

The main computation burden is vector addition operation, which has the complexity around $O(N_xN_yN_z)$.

In total, for Algorithm 3 or 4, its main computation complexity is about $O\left(\left(N_xN_yN_z\right)^3\right)$.

Appendix A.3. Algorithm 5

Similar to Algorithms 3 and 4, the proposed algorithm solves the same three sub-problems in each iteration. The second and third ones are solved by the same means. Thus, it has the same computation complexity of $O(N_xN_yN_z)$. To reduce the complexity from the matrix-vector multiplication and matrix inverse operations, two modifications are proposed. The first one is to linearize the original problem and solve it with gradient descent instead of matrix inverse. The second one is to embed the imaging operator and its adjoint to approximate the system sensing matrix. Thus, the first sub-problem is solved as

$$\begin{aligned}\mathbf{x}_k &= \mathbf{x}_{k-1} - \frac{1}{L}[\lambda\mathbf{x}_{k-1} + I(g(\mathbf{x}_{k-1})) - I(y) - \lambda(\mathbf{v}_{k-1} + \mathbf{d}_{k-1})]\\ &\approx \mathbf{x}_{k-1} - \frac{1}{L}[\lambda\mathbf{x}_{k-1} + \mathbf{x}_{k-1} - y_{MF} - \lambda(\mathbf{v}_{k-1} + \mathbf{d}_{k-1})]\end{aligned} \tag{A9}$$

The main computation burden is vector addition operation, which has the complexity around $O(N_xN_yN_z)$. In total, for the proposed algorithm, its main computation complexity is about $O(N_xN_yN_z)$.

References

1. Wu, J.; Sun, Z.; An, H.; Qu, J.; Yang, J. Azimuth Signal Multichannel Reconstruction and Channel Configuration Design for Geosynchronous Spaceborne–airborne Bistatic SAR. *IEEE Trans. Geosci. Remote Sens.* **2018**, *57*, 1861–1872. [CrossRef]
2. Wang, Z.M.; Guo, Q.J.; Tian, X.Z. 3-D Millimeter-wave Imaging Using MIMO RMA with Range Compensation. *IEEE Trans. Microw. Theory Tech.* **2019**, *67*, 1157–1166. [CrossRef]
3. Moses, R.L.; Potter, L.C.; Çetin, M. Wide Angle SAR Imaging. In Proceedings of the 2004 International Society for Optics and Photonics in Defense and Security, Orlando, FL, USA, 12–16 April 2004; pp. 164–175.
4. Zhou, L.; Zhang, X.; Pu, L.; Zhang, T.; Shi, J.; Wei, S. A High-Precision Motion Errors Compensation Method Based on Sub-Image Reconstruction for HRWS SAR Imaging. *Remote Sens.* **2022**, *14*, 1033. [CrossRef]
5. Xu, Z.; Zhang, B.; Zhou, G.; Zhong, L.; Wu, Y. Sparse SAR Imaging and Quantitative Evaluation Based on Nonconvex and TV Regularization. *Remote Sens.* **2021**, *13*, 1643. [CrossRef]
6. Zhang, Q.; Zhang, Y.; Zhang, Y.; Huang, Y.; Yang, J. A Sparse Denoising-Based Super-Resolution Method for Scanning Radar Imaging. *Remote Sens.* **2021**, *13*, 2768. [CrossRef]
7. Wang, Y.; Zhang, X.; Zhan, X.; Zhang, T.; Zhou, L.; Shi, J.; Wei, S. An RCS Measurement Method Using Sparse Imaging Based 3D SAR Complex Image. *IEEE Antennas Wirel. Propag. Lett.* **2022**, *21*, 24–28. [CrossRef]
8. Wang, M.; Wei, S.; Liang, J.; Liu, S.; Shi, J.; Zhang, X. Lightweight FISTA-Inspired Sparse Reconstruction Network for mmW 3-D Holography. *IEEE Trans. Geosci. Remote Sens.* **2022**, *60*, 1–20. [CrossRef]
9. Salvetti, F.; Martorella, M.; Giusti, E. Multi-view Three-dimensional Interferometric Inverse Synthetic Aperture Radar. *IEEE Trans. Aerosp. Electron. Syst.* **2018**, *55*, 718–733. [CrossRef]
10. Oveis, A.H.; Guisti, E.; Ghio, S.; Martorella, M. A Survey on the Applications of Convolutional Neural Networks for Synthetic Aperture Radar: Recent Advances. *IEEE Aerosp. Electron. Syst. Mag.* **2021**. [CrossRef]
11. Huang, L.; Liu, B.; Li, B.; Guo, W.; Yu, W.; Zhang, Z.; Yu, W. OpenSARShip: A dataset dedicated to Sentinel-1 ship interpretation. *IEEE J. Sel. Top. Appl. Earth Observ. Remote Sens.* **2018**, *11*, 195–208. [CrossRef]
12. Li, J.; Qu, C.; Shao, J. Ship detection in SAR images based on an improved faster R-CNN. In Proceedings of the 2017 SAR in Big Data Era: Models, Methods and Applications (BIGSARDATA), Beijing, China, 13–14 November 2017; pp. 1–6.
13. Liu, N.; Cao, Z.; Cui, Z.; Pi, Y.; Dang, S. Multi-Scale Proposal Generation for Ship Detection in SAR Images. *Remote Sens.* **2019**, *11*, 526. [CrossRef]
14. Wei, S.; Zhou, Z.; Wang, M.; Wei, J.; Liu, S.; Shi, J.; Zhang, X.; Fan, F. 3DRIED: A High-Resolution 3-D Millimeter-Wave Radar Dataset Dedicated to Imaging and Evaluation. *Remote Sens.* **2021**, *13*, 3366. [CrossRef]
15. Bamler, R. A Comparison of Range-Doppler and Wavenumber Domain SAR Focusing Algorithms. *IEEE Trans. Geosci. Remote Sens.* **1992**, *30*, 706–713. [CrossRef]
16. Hu, C.; Wang, L.; Zhu, D.; Loffeld, O. Inverse Synthetic Aperture Radar Sparse Imaging Exploiting the Group Dictionary Learning. *Remote Sens.* **2021**, *13*, 2812. [CrossRef]
17. Patel, V.M.; Easley, G.R., Jr.; Healy, D.M.; Chellappa, R. Compressed Synthetic Aperture Radar. *IEEE J. Sel. Top. Signal Process.* **2010**, *4*, 244–254. [CrossRef]
18. Selesnick, I. Sparse Regularization via Convex Analysis. *IEEE Trans. Signal Process.* **2017**, *65*, 4481–4494. [CrossRef]
19. Baraniuk, R.; Steeghs P. Compressive Radar Imaging. In Proceedings of the IEEE Radar Conference, Waltham, MA, USA, 17–20 April 2007; pp. 128–133.
20. Daubechies, I.; Defriese, M.; De Mol, C. An Iterative Thresholding Algorithm for Linear Inverse Problems with A Sparsity Constraint. *Commun. Pure Appl. Math.* **2004**, *57*, 1413–1457. [CrossRef]
21. Beck, A.; Teboulle, M. A Fast Iterative Shrinkage-Thresholding Algorithm for Linear Inverse Problems. *SIAM J. Imaging Sci.* **2009**, *2*, 183–202. [CrossRef]
22. Boyd, S.; Parikh, N.; Chu, E.; Peleato, B.; Eckstein, J. *Distributed Optimization and Statistical Learning via The Alternating Direction Method of Multipliers*; Foundations and Trends® in Machine Learning: Berkeley, CA, USA, 2011; Volume 3, pp. 1–122.
23. Candes, E.; Tao, T. The Dantzig Selector: Statistical Estimation When p Is much Larger Than n. *Ann. Stat.* **2007**, *35*, 2313–2351.
24. Osher, S.; Ruan, F.; Xiong, J.; Yao, Y.; Yin, W. Sparse Recovery via Differential Inclusions. *Appl. Comput. Harmon. Anal.* **2016**, *41*, 436–469. [CrossRef]
25. Fan, J.; Li, R. Variable Selection via Nonconcave Penalized Likelihood and Its Oracle Properties. *J. Am. Stat. Assoc.* **2001**, *96*, 1348–1360. [CrossRef]
26. Zhang, C.-H. Nearly Unbiased Variable Selection under Minimax Concave Penalty. *Ann. Stat.* **2010**, *38*, 894–942. [CrossRef]
27. Yao, J.; Meng, D.; Zhao, Q.; Cao, W.; Xu, Z. Nonconvex-Sparsity and Nonlocal-Smoothness-Based Blind Hyperspectral Unmixing. *IEEE Trans. Image Process.* **2019**, *28*, 2991–3006. [CrossRef] [PubMed]
28. Yao, J.; Hong, D.; Xu, L.; Meng, D.; Chanussot, J.; Xu, Z. Sparsity-Enhanced Convolutional Decomposition: A Novel Tensor-Based Paradigm for Blind Hyperspectral Unmixing. *IEEE Trans. Geosci. Remote Sens.* **2022**, *60*, 5505014. TGRS.2021.3069845. [CrossRef]
29. Zuo, W.; Meng, D.; Zhang, L.; Feng, X.; Zhang, D. A Generalized Iterated Shrinkage Algorithm for Non-convex Sparse Coding. In Proceedings of the 2013 IEEE International Conference on Computer Vision, Sydney, NSW, Australia, 1–8 December 2013; pp. 217–224.

30. Wang, Y.; He, Z.; Zhan, X.; Fu, Y.; Zhou, L. Three-Dimensional Sparse SAR Imaging with Generalized L_q Regularization. *Remote Sens.* **2022**, *14*, 288. [CrossRef]

31. Woodworth, J.; Chartrand, R. Compressed Sensing Recovery via Nonconvex Shrinkage Penalties. *Inverse Probl.* **2016**, *32*, 075004. [CrossRef]

32. Nikolova, M.; Ng, M.K.; Tam, C.-P. Fast Nonconvex Nonsmooth Minimization Methods for Image Restoration and Reconstruction. *IEEE Trans. Image Process.* **2010**, *19*, 3073–3088. [CrossRef]

33. Parekh, A.; Selesnick, I.W. Convex Denoising Using Non-convex Tight Frame Regularization. *IEEE Signal Process. Lett.* **2015**, *22*, 1786–1790. [CrossRef]

34. Lanza, A.; Morigi, S.; Sgallari, F. Convex Image Denoising via Non-convex Regularization with Parameter Selection. *J. Math Imaging Vis.* **2016**, *56*, 195–220. [CrossRef]

35. Selesnick, I. Total Variation Denoising via The Moreau Envelope. *IEEE Signal Process. Lett.* **2017**, *24*, 216–220. [CrossRef]

36. Selesnick, I.; Lanza, A.; Morigi, S.; Sgallari, F. Non-convex Total Variation Regularization for Convex Denoising of Signals. *J. Math. Imaging Vis.* **2020**, *62*, 825–841. [CrossRef]

37. Liu, Y.; Du, H.; Wang, Z.; Mei, W. Convex MR Brain Image Reconstruction via Non-convex Total Variation Minimization. *Int. J. Imaging Syst. Technol.* **2018**, *28*, 246–253. [CrossRef]

38. Anantrasirichai, N.; Zheng, R.; Selesnick, I.; Achim, A. Image Fusion via Sparse Regularization with Non-convex Penalties. *Pattern Recognit. Lett.* **2020**, *131*, 355–360. [CrossRef]

39. Karakuş, O.; Mayo, P.; Achim, A. Convergence Guarantees for Non-Convex Optimisation with Cauchy-based Penalties. *IEEE Trans. Signal Process.* **2020**, *131*, 355–360. [CrossRef]

40. Afonso, M.; Bioucas-Dias, J.M.; Figueiredo, M.A.T. Fast Image Recovery Using Variable Splitting and Constrained Optimization. *IEEE Trans. Image Process.* **2010**, *10*, 2345–2356. [CrossRef] [PubMed]

41. Afonso, M.; Bioucas-Dias, J.M.; Figueiredo, M.A.T. An Augmented Lagrangian Approach to the Constrained Optimization Formulation of Imaging Inverse Problems. *IEEE Trans. Image Process.* **2011**, *20*, 681–695. [CrossRef]

42. Wahlberg, B.; Boyd, S.; Annergren, M.; Wang, Y. An ADMM Algorithm for A Class of Total Variation Regularized Estimation Problems. In Proceedings of the 16th IFAC Symposium System Identification, Brussels, Belgium, 5 May 2012; pp. 83–88.

43. Wan, T.; Canagarajah, N.; Achim, A. Segmentation of Noisy Colour Images Using Cauchy Distribution in The Complex Wavelet Domain. *IET Image Process.* **2011**, *5*, 159–170. [CrossRef]

44. Nocedal, J; Wright, S.J. *Numerical Optimization*, 2nd ed.; Springer: New York, NY, USA, 2006.

45. Boyd, S.; Parikh, N. Proximal algorithms. *Found. Trends Optim.* **2014**, *1*, 127–239.

46. Fang, J.; Xu, Z.; Zhang, B.; Hong, W.; Wu, Y. Fast Compressed Sensing SAR Imaging Based on Approximated Observation. *IEEE J. Sel. Top. Appl. Earth Observ.* **2014**, *7*, 352–363. [CrossRef]

47. Bi, H.; Bi, G.; Zhang, B.; Hong, W. Complex-Image-Based Sparse SAR Imaging and Its Equivalence. *IEEE Trans. Geosci. Remote Sens.* **2018**, *56*, 5006–5014. [CrossRef]

48. Han, Y.; Ye, J.C. Framing U-Net via Deep Convolutional Framelets: Application to Sparse-view CT. *IEEE Trans. Med. Imaging* **2018**, *37*, 1418–1429. [CrossRef] [PubMed]

49. Xu, Z.; Wei, Z.; Liu, M.; Zhang, B.; Wu, Y. Analysis and Suppression of Bias Effect in Sparse SAR Imaging. In *Image and Signal Processing for Remote Sensing XXV*; International Society for Optics and Photonics: Bellingham, WA, USA, 2019; p. 111551E.

50. Yang, L.; Zhang, S.; Fang, C.; Wu, R.; Han, P.; Xing, M. Structure-Awareness SAR Imagery by Exploiting Structure Tensor TV Regularization Under Multitask Learning Framework. *IEEE Trans. Geosci. Remote Sens.* **2022**, *60*, 5203315. [CrossRef]

51. Combettes, P. L.; Pesquet, J.-C. Proximal splitting methods in signal processing. In *Fixed-Point Algorithms for Inverse Problems in Science and Engineering*; Springer: New York, NY, USA, 2011; pp. 185–212.